

# A Primal Sketch of the Cortex Mean Curvature: A Morphogenesis Based Approach to Study the Variability of the Folding Patterns

A. Cachia\*, J.-F. Mangin, D. Rivière, F. Kherif, N. Boddaert, A. Andrade, D. Papadopoulos-Orfanos, J.-B. Poline, I. Bloch, M. Zilbovicius, P. Sonigo, F. Brunelle, and J. Régis

**Abstract**—In this paper, we propose a new representation of the cortical surface that may be used to study the cortex folding process and to recover some putative stable anatomical landmarks called *sulcal roots* usually buried in the depth of adult brains. This representation is a primal sketch derived from a scale space computed for the mean curvature of the cortical surface. This scale-space stems from a diffusion equation geodesic to the cortical surface. The primal sketch is made up of objects defined from mean curvature minima and saddle points. The resulting sketch aims first at highlighting significant elementary cortical folds, second at representing the fold merging process during brain growth. The relevance of the framework is illustrated by the study of central sulcus sulcal roots from antenatal to adult age. Some results are proposed for ten different brains. Some preliminary results are also provided for superior temporal sulcus.

**Index Terms**—Morphometry, spatial normalization, sulcogenesis, variability.

## I. INTRODUCTION

THE ADVENT of methods dedicated to the automatic analysis of large databases of magnetic resonance images (MRIs) images of brain anatomy has raised a large interest in the neuroscience community [1]–[12]. These tools, indeed, provide new ways of addressing issues related to the compar-

ison of brain populations. They allow the study of the influence of various parameters (sex, dominant hemisphere, cognitive features, genetic features, pathology, etc.) on the anatomical *substratum* [13]–[17]. Longitudinal studies of brain maturation or aging process have also received increasing attention [18]–[20]. The complexity and the interindividual variability of the cortical folding patterns, however, is still a challenging issue for these tools. Indeed, nobody really knows how to match the cortical folds across brains and at which extent such a matching is relevant from a neuroscience point of view.

### A. Spatial Normalization

Most of the brain anatomy analysis methods rely on the concept of spatial normalization, which consists in warping all the brains toward a template endowed with a three-dimensional (3-D) (volumetrical) or a two-dimensional (2-D) (spherical) coordinate system. This referential then underlies further statistical studies. This coordinate-based spatial normalization paradigm has made a tremendous impact on morphometry strategies because of its versatility. A number of different normalization algorithms, however, are used throughout the world, each one potentially leading to different results. For instance, the widely distributed SPM software (<http://www.fil.ion.ucl.ac.uk/spm/> [4], [7]) allows the user to choose the template or the number of basis functions used to model the warping. This observation means that what is called spatial normalization is far from being clear, which is explained by the fact that nobody really knows what may be the gold standard in terms of brain warping. Furthermore, nobody knows today to which extent matching two different brains with a continuous deformation makes sense from an anatomical point of view.

With regards to the problems induced by the variability of the cortical folding patterns, recent hypotheses claim that some answers could stem from a better understanding of the brain growth processes [21], [22]. This paper proposes a new representation of the cortical surface that aims at highlighting some of the fold merging events that occur during the cortical surface folding process.

### B. Gyrogenesis and Sulcal Variability

Cortical folding, the gross anatomical landmarks of the cortical surface, exhibit various forms in different adult brains [23], which prevents from using them as a straightforward and accurate referential. The origin and meaning of this variability are still largely unclear and discussed [22], [24]. Nevertheless, a

Manuscript received June 25, 2002; revised February 3, 2003. Asterisk indicates corresponding author.

\*A. Cachia is with the Service Hospitalier Frédéric Joliot, CEA, 4, place du Gal Leclerc, 91401 Orsay, Cedex, France. He is also with the Département Traitement du Signal et des Images, CNRS U820, ENST, 75013 Paris, France; the Institut Fédératif de Recherche 49, Paris, France; Brain Imaging in Psychiatry team, INSERM ERM205, Orsay, France and the Institut Fédératif de Recherche 49, Paris, France (e-mail: cachia@shfj.cea.fr).

J.-F. Mangin, J.-B. Poline, and M. Zilbovicius are with the Service Hospitalier Frédéric Joliot, CEA, 91401 Orsay, Cedex, France. They are also with the Brain Imaging in Psychiatry team, INSERM ERM205, Orsay, France and the Institut Fédératif de Recherche 49, Paris, France.

D. Rivière, F. Kherif, A. Andrade, and D. Papadopoulos-Orfanos are with the Service Hospitalier Frédéric Joliot, CEA, 91401 Orsay, Cedex, France. They are also with the Institut Fédératif de Recherche 49, Paris, France.

N. Boddaert is with the Service de Radiologie Pédiatrique, Necker Hospital, 75743 Paris, France. She is also with the Brain Imaging in Psychiatry team, INSERM ERM205, Orsay, France, and the Institut Fédératif de Recherche 49, Paris, France.

I. Bloch is with the Département Traitement du Signal et des Images, CNRS U820, ENST, 75013 Paris, France. She is also with the Institut Fédératif de Recherche 49, Paris, France.

P. Sonigo and F. Brunelle are with the Service de Radiologie Pédiatrique, Necker Hospital, 75743 Paris, France. They are also with the Institut Fédératif de Recherche 49, Paris, France.

J. Régis is with the Service de Neurochirurgie Fonctionnelle et Stereotaxique, La Timone Hospital, 13005 Marseille, France.

Digital Object Identifier 10.1109/TMI.2003.814781

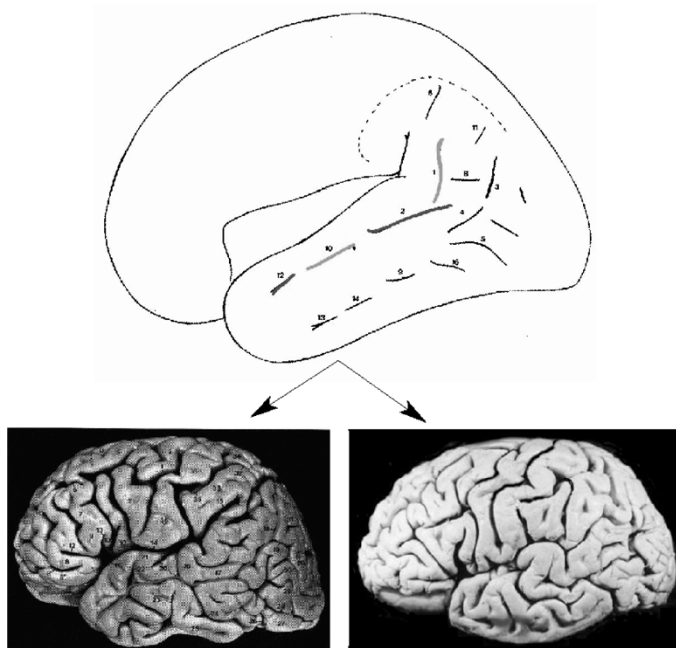


Fig. 1. Top: A map of the first fetal cortical folds (sulcal roots) of the temporal lobe [25]. The folds are numerated according to their date of appearance during the fetal sulcogenesis. Different merging events between these sulcal roots can lead to very different folding patterns at adult age. Bottom left: The superior temporal sulcus is supposed to stem from the merge of four different sulcal roots. Bottom right: The usual merging events leading to the superior temporal sulcus have not occurred.

bundle of converging arguments, stemming from ontogenesis, phylogenesis, and architectonic considerations, have led to hypothesize that a simple and stable organization of the folding, related to the fetal stage, may underlie the apparently variable and intricate sulcal patterns of adult cortices [21], [25]. Indeed, the first cortical folds that appear on the fetus cortex, called *sulcal roots*, seem to be especially *stable* (in number, position, and orientation) across individuals. During the following gyral expansion, however, these sulcal roots become buried into the depth of the cortex after having merged with each other to build larger folds. Because *variable merging events* can occur, different sulcal patterns can be observed at adult age (see Fig. 1). The more usual patterns have led to the standard sulcus nomenclature [23], but some brains are very difficult to read according to this nomenclature, either because the main sulci are split into pieces or worst because the sulcal root merge events have created unusual sulci.

One of the simplest examples of sulcus, which will be used to illustrate the method described in this paper, is the central sulcus (see Fig. 2). This large sulcus is a very interesting landmark on the cortical surface because it is the limit between motor and somesthetic areas. Hence, the study of its shape has been the subject of numerous studies [17], [26]–[29]. The central sulcus is supposed to be made up of two sulcal roots that merge in almost all cases. In very rare cases, however, this merge does not occur and the central sulcus is split in the middle by a gyrus [30], [31]. Nevertheless, in most of the noninterrupted cases, this gyrus is still visible on the walls of the sulcus [32]–[34]. This gyrus initially separating the two sulcal roots, indeed, has just been buried into the depth of the cortex. Hence, a stable simple fetal pattern seems

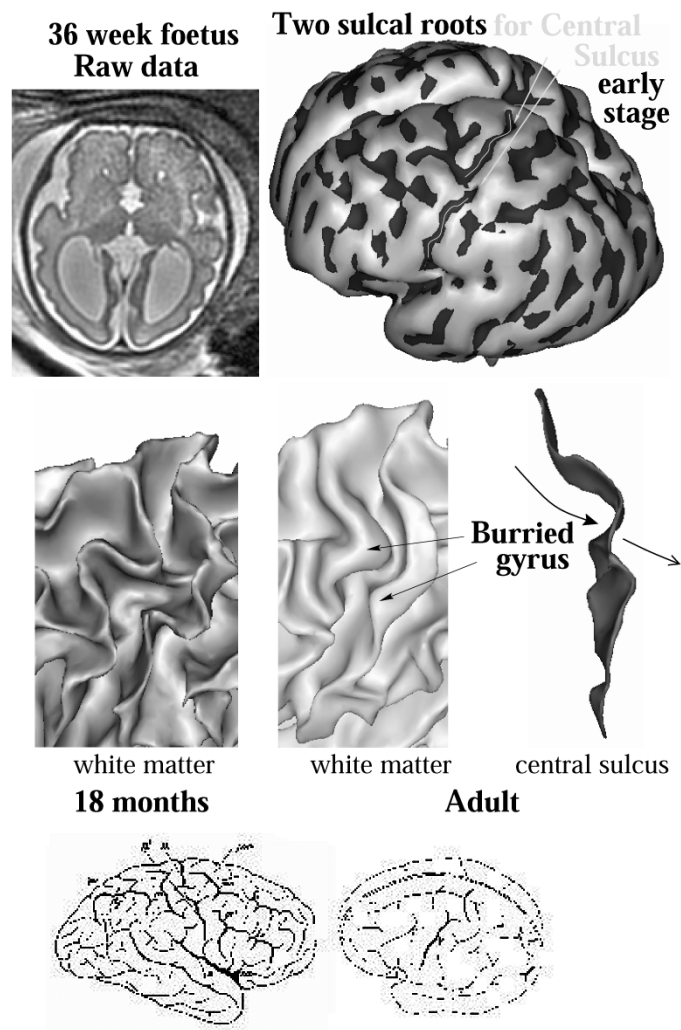


Fig. 2. Evolution of the central sulcus shape during brain growth. Top: Antenatal images allow the reconstruction of the fetus cortex surface on which shallow dimples corresponding to negative mean curvature areas are highlighted in dark. At that stage, the central sulcus is made up of two sulcal roots. Middle left: 18 months after birth, the gyrus separating the two sulcal roots is still visible on white matter surface. Middle right: At adult stage, only slight deformations of the central sulcus walls give clues on the presence of a buried gyrus. Bottom: In some rare brains described in literature, the two sulcal roots of the central sulcus have not merged [30], [31].

to make the link between all the possible configurations. This paper aims at developing a method inferring this primal pattern from local information about the curvature of sulcal walls and fundi, which gives clues about the localization of the sulcal roots. Surface curvature, indeed, embeds more information than the geodesic depth that has been previously proposed to segment sulci into smaller units [35], [36].

In the following, we propose a new representation of the cortical surface that may be used to study the cortex folding process and to recover putative stable anatomical landmarks, the sulcal roots, usually buried in the depth of adult brains. This representation is a primal sketch [37], [38] derived from a scale space [39], [40] computed for the mean curvature of the cortical surface. This scale-space stems from a diffusion process geodesic to the cortical surface. The primal sketch is made up of objects defined from mean curvature minima and saddle points, like in previous approaches [41], [42]. The resulting sketch aims first

at highlighting significant elementary folds, second at representing the fold merging process during brain growth.

The long term aim of the method consists in recovering automatically a map of the sulcal roots from any adult brain. This map would provide an appealing set of landmarks to match different adult folding patterns. The sulcal roots could then be used to add some reliable constraints into standard warping algorithms [43]–[46]. Such a map could also be used to study brain development from antenatal MR images. Statistics on sulcal root chronology of appearance may indeed become a precious tool for early detection of development problems. Some interesting cognitive or clinical information could also be embedded into the variable merging events occurring between the sulcal roots. Finally, since the sulcal roots are defined as indivisible cortical folds, they could be used to overcome the problem induced by sulcus interruption in algorithmic approaches relying on one-dimensional (1-D) lines [47] or 2-D meshes [48], [49].

## II. FOLDING PROCESS AND CURVATURE

The first stage of the method consists in extracting a smooth mesh representing the cortical surface of each hemisphere from a T1-weighted MR image. This mesh is endowed with the actual spherical topology of this surface, which allows the implementation of geodesic diffusion and inflation operations.

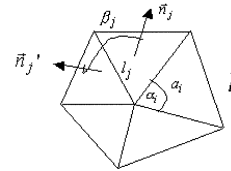
### A. Spherical Triangulation of Cortical Hemispheres

A first sequence of treatments provides a binary mask of each hemisphere cortex with spherical homotopy. This sequence, which includes bias correction [50], brain mask segmentation [51], hemisphere mask segmentation [52], and detection of the gray/white interface [53], is freely available on “<http://anatomist.info>.” A standard facet tracking algorithm is used to compute a first spherical mesh made up of facets from the cortex mask [54]. Then, the center of each facet is connected to the center of the neighboring facets in order to yield a spherical mesh of triangles. This algorithm, which preserves the initial spherical topology, relies on a look-up table of configurations like in the standard marching cube algorithm. Finally, a decimation including smoothing is performed to discard stair artifacts related to the underlying discretization. The decimation algorithm is inspired by the algorithm used in the visualization toolkit (VTK) package [55]. The embedded smoothing operation iteratively moves the nodes toward their neighborhood gravity center, which may be related to some usual surface evolution processes [58].

This mesh construction includes some smoothing operations that may remove some interesting anatomical information. Nevertheless, this smoothing process is required to get initial acceptable surface representations and reliable mean curvature estimations. In the future, surface evolution approaches could provide alternative scale-space computation that might be less restrictive.

### B. Mean Curvature Estimation

Different approaches can be used to describe and study fine details of the cortical surface folding patterns. Depth maxima have been used to detect a concept similar to sulcal roots in



$$H = \frac{\frac{1}{4} \sum_j \beta_j l_j}{\frac{1}{2} \sum_i a_i - \frac{1}{8} \sum_i l_i^2 \cot(\alpha_i)}$$

Fig. 3. Approximation of the mean curvature from an irregular mesh [60].  $\alpha_i$  and  $a_i$  denote, respectively, the triangle angles and areas;  $\beta_j$  correspond to the dihedral angles between the normals  $n_j$ ; the edge lengths are noted  $l_i$ .

[35]. In this paper, mean curvature ( $H$ ) is proposed as a richer descriptor (than the depth) of the various features that can be observed along sulcus bottoms and walls, which is illustrated in Fig. 8: fold bottoms appear as local minima of  $H$ , while gyrus crowns appear as local maxima. Hence, buried gyri separating two *sulcal roots*, appear as areas of positive curvature along the sulcus walls. Other curvature related features, such as Koenderink’s curvature metric  $C$  (the L2 norm of the principal curvatures, or the logarithm thereof) or the maximum principal curvature, may be interesting for our purpose and should be investigated in the future. It should be noted that an isophote mean curvature related measure ( $L_{vv}$ ) has also been proposed to distinguish sulci from gyri [48]. While this approach could be used to get a mean curvature estimation related to our cortical surface representation (which may be considered as one given isophote), its main interest is in the definition of gyrus and sulcus skeletons as surfaces of singularities [74].

In this paper, mean curvature is directly estimated from the mesh thanks to its relative smoothness. We used an approximation proposed in [60] and [61] that takes into account some local properties of the mesh, as triangle angles  $\alpha_i$  and areas  $a_i$ , dihedral angles  $\beta_j$  between normals  $\vec{n}_j$  and edge lengths  $l_i$  (see Fig. 3). This method may be considered as less robust than the usual quadratic patch-based approaches, but was chosen in this paper for its lower computational burden. It should be noted that it is too soon to claim that one kind of curvature-based map is more adapted to our purpose than another one.

### C. Fetus and Baby Brains

The previous chain of processing is used when the brain has reached a high level of myelination of axons, namely for more than two years old brains. At this stage, indeed, standard T1-weighted images based on inversion recovery sequences give a good contrast between gray and white matter, leading to an accurate definition of the cortical inner surface. Since the most interesting part of the folding process is during antenatal stage, however, we have initiated a research program aiming at performing longitudinal studies from antenatal MR images obtained from clinical studies.

In the case of antenatal and small baby brains, however, the axon myelination is still in progress, which means that T1-weighted images show more or less contrast between gray and white matters according to the brain areas. Therefore, we have adapted the previous chain of processing to T2-weighted images, which provide a better contrast (see Fig. 2) [62]. Unfortunately, T2-weighted images usually have a larger slice thickness, especially with antenatal imaging, where acquisitions have to be very fast because of the fetus frequent

motions and for his mother comfort. Since the fetus brains are very small, this is leading to partial volume problems in the definition of the cortical inner surface. Hence, we have chosen to study the cortex outer surface, which is located between the cerebro spinal fluid and the brain tissues. It should be noted, however, that the structural study of the folding process can be done from the cortex outer surface as from the inner surface, as far as the surface representation is reliable.

The current segmentation toolbox is semiautomatic and is still far to yield perfect results. Anyway, designing a perfect surface detection method is a challenge because of the frequent artifacts induced by fetus motions and the various contrast modifications during the myelinization. Nevertheless, for a few fetus brains, the detected surfaces are sufficiently clean to visualize small dimples bound to become cortical folds as connected components of negative curvature (see Fig. 2). These images allow us to question the first sulcal root maps, which had been inferred from various descriptions of the literature (see Fig. 1) [25]. Unfortunately, the various weaknesses of the current acquisition process lead to an awful percentage of success: one acquisition over 100 can provide a meaningful cortical surface representation. Hence, we are currently working on faster acquisition schemes using new MR sequences [56] and multicoil approaches [57], because the main problem to be solved is motion between slices. In the future, longitudinal acquisitions at several time steps could allow to follow the folding process subject by subject, provided that such studies are ethically acceptable.

### III. SCALE SPACE OF THE CURVATURE MAP

The curvature map of the cortical surface contains much geometrical information that may be related to the anatomical elements that have to be detected (sulcal roots, buried gyri). These elements, however, correspond to different levels of scale (see Fig. 9). Moreover, a scale-based point of view is required to distinguish anatomical elements from noise features bound to appear in curvature approximations, due to segmentation/triangulation artifacts, or biased estimations of the discrete curvature (see Fig. 8). The scale-space paradigm has been developed to deal with such problems where all the scales may be of interest.

#### A. Geodesic Diffusion of the Curvature Map

Two alternative approaches can be used to create a family of curvature maps evolving toward smoothness, either a diffusion process geodesic to the cortical surface [63], [64], or a geometric evolution of the surface itself [58]. Surface evolution according to a function of curvature has been widely used in image analysis to describe 3-D shapes. The standard implementation of this kind of evolution using the level set framework, however, is not adapted to our goal. This framework, indeed, allows topological modifications of the tracked isosurface and provides no constant parameterization that may be used to simply track objects across scales. A mesh-based implementation, in return, may be used for the evolution process, but would not necessarily be providing the causality property required to deal with the scale space [39], [40]. At each iteration, indeed, some curvature estimation errors would be made. It should be noted, however, that such an imple-

mentation is used to inflate the cortical surface for visualization purpose [59].

In the following, the scale space of the curvature map is computed from the heat equation [40] geodesically to the cortical surface. This is an arbitrary choice made to experiment with the anatomical structural ideas mentioned above. A few experiments using inflated versions of the initial surface to compute the geodesic diffusion have shown few consequences on the sulcal structures of interest in the scale space. Some more studies have to be done, however, to get a better idea of the influence of the intrinsic curvature of the cortex on the diffusion process [65]. In the future, the behavior of alternative anisotropic diffusion schemes [66] could also be considered. For instance, further work could consist in looking for the diffusion scheme maximizing the similarity across subjects of the structural representations inferred from the individual scale spaces.

The heat equation, which corresponds to a parabolic partial differential equation (PDE), lends itself with relative ease to being adapted for the specific case of an irregular 2-D lattice embedded in a 3-D space [63], [64].

#### B. Numerical Implementation

The numerical implementation of the heat equation is carried out as an iterative process of the form

$$\frac{H(M, t + \delta t) - H(M, t)}{\delta t} = \widehat{\Delta H}(M, t) \quad (1)$$

for each node  $M$  and each temporal iteration step  $\delta t$ , where  $\widehat{\Delta H}$  is the Laplacian estimate at the node  $M$  of the field of values (i.e., the map  $H$  of the curvature).

The implementation of PDEs on irregular lattices can lead to complex numerical problems; the *causality* property usually required by the scale-space framework may be lost because of discrete phenomena. This point is beyond the scope of this paper and would require further study.

1) *Spatial Parameterization*: The fact that the cortical lattice is embedded into a volume raises a question concerning the proper axis system upon which to base the estimation of the local partial derivatives. A conflict exists between the need to employ three spatial coordinates in the Euclidean space to obtain an ambiguity-free description of the position of each node, and the wish to perform a strictly surface-based smoothing. The definition of a coordinate system intrinsic to the surface would allow for a strictly 2-D-based smoothing. This implies a parameterization, i.e., the definition of a mapping function  $m$  such that  $(x, y, z) \equiv m(u, v)$ ,  $u$  and  $v$  being the new coordinates that allow to refer to every point in the surface without ambiguity. The diffusion equation is then solved along  $u$  and  $v$ , in a strictly 2-D fashion.

A possible parameterization would consist in the application of a flattening procedure to the cortical lattice representation [59]. This way, the flattened cortex would be contained in a plane, and the parameterized coordinates  $(u, v)$  would correspond simply to the  $(x', y')$  coordinates of the plane in question. However, cortical flattening leads to a significant amount of metric distortion (10%–20% in average, locally attaining much

higher values [6], [59]) and requires the introduction of cuts because of the cortex spherical topology. Using the mapping to a sphere would be an alternative solution [8], but spherical coordinates include two poles leading to some other difficulties.

2) *Local Planar Parameterization*: In view of this, the adopted parameterization was a simple *local* transformation that maps each surface element (a node and its first neighbors) into a plane, while keeping unchanged both the edge distances and the angular proportions between the edges. This “neighborhood parameterization” [69], [70] amounts to locally flatten the surface element, and avoids the severe areal distortion that would result from an explicit *global* flattening.

An individual mapping function  $m_i$  is, thus, defined for each node  $i$ , independently of the surrounding surface elements. An arbitrarily oriented orthogonal referential is defined for each surface element, centered at its central node, and all the required estimations, notably local Laplacian, are based on this new coordinate system. This local-based approach is made possible since, for each iteration step of the numerical solution of the diffusion equation, the estimations involve only the differences between the values associated with each node and its nearest neighbors.

3) *Estimation of the Laplacian Operator*: The adopted (finite-difference) approach [71], [72] assumes that the field, implicitly described by the function  $H(u, v)$ , is now sampled with an irregular planar lattice composed of interconnected nodes. A Taylor series expansion around a given point  $(u_c, v_c)$  has the form

$$H_i = H_c + h_i \frac{\partial H_c}{\partial u} + k_i \frac{\partial H_c}{\partial v} + \frac{h_i^2}{2} \frac{\partial^2 H_c}{\partial u^2} + \frac{k_i^2}{2} \frac{\partial^2 H_c}{\partial v^2} + k_i h_i \frac{\partial^2 H_c}{\partial u \partial v} + O(\delta^3) \quad (2)$$

where  $H_c = H(u_c, v_c)$ ,  $H_i = H(u_i, v_i)$ ,  $\partial H_c / \partial u$ , and  $\partial H_c / \partial v$  denote the partial derivative of  $H(u, v)$  at point  $(u_c, v_c)$ ,  $h_i = u_i - u_c$ ,  $k_i = v_i - v_c$ , and  $\delta = \sqrt{h_i^2 + k_i^2}$ . Writing (2) for a surface element consisting of a central lattice node, located at  $(u_c, v_c)$ , and its neighbors  $(u_i, v_i)$   $i = 1, 2, \dots, m$  leads to

$$AD - H = [0]$$

where

$$A = \begin{bmatrix} h_1 & k_1 & \frac{h_1^2}{2} & \frac{k_1^2}{2} & h_1 k_1 \\ h_2 & \dots & \dots & \dots & \dots \\ \vdots & & & & \\ \vdots & & & & \\ h_m & & & & \end{bmatrix}$$

$$H = [H_1 - H_c, H_2 - H_c, \dots, H_m - H_c]^T$$

and the five derivatives at  $(u_c, v_c)$  are

$$D = \left[ \frac{\partial H_c}{\partial u}, \frac{\partial H_c}{\partial v}, \frac{\partial^2 H_c}{\partial u^2}, \frac{\partial^2 H_c}{\partial v^2}, \frac{\partial^2 H_c}{\partial u \partial v} \right]^T.$$

In this fashion, estimates of the 2-D Laplacian ( $\Delta H(u, v) = (\partial^2 H / \partial u^2) + (\partial^2 H / \partial v^2)$ ) are obtained at each node of the lat-

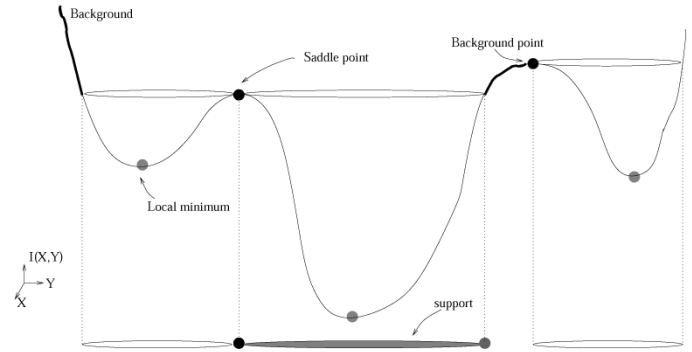


Fig. 4. Definition of GLBs from local minima and saddle points (2-D case).

tice. This approach amounts to solving, for each node, a linear system involving the relative positions of the node and its neighbors and the corresponding field value differences. It is still a finite-differences method, in the sense that the partial derivatives are estimated by differences between field values in neighboring points, but its range of application is extended to any arbitrarily irregular grid. The resolution of the system, for each node, is done in a least-squares fashion

$$D = A^{-1}H. \quad (3)$$

This system of equations is solved *once for each node* at the beginning of the diffusion process.

Practically, the estimation of the Laplacian operator at each mesh node entails the multiplication of the pseudoinverse estimation ( $A^-$ ) of the matrix  $A$  by the vector containing the differential data  $(u_1 - u_c, u_2 - u_c, \dots, u_m - u_c)$ , with  $m$  denoting the number of neighbors [71]

$$\widehat{\Delta H}_i = \frac{\partial^2 H_c}{\partial u^2} + \frac{\partial^2 H_c}{\partial v^2} = \sum_{i=1}^m \omega_i * (u_i - u_c) \quad (4)$$

with  $\omega_i = A_{3i}^- + A_{4i}^-$ , where  $A_{ki}^-$  denotes the element on the  $k$ rd line and  $i$ th column of the pseudoinverse matrix.

#### IV. PRIMAL SKETCH OF THE CURVATURE MAP

A primal sketch is constructed from the curvature map using the algorithm proposed by Lindeberg in [42]. This primal sketch is expected to exhaustively describe the structure of the scale space of the curvature map and, therefore, to pinpoint its relevant embedded objects. These objects are valleys of the curvature landscape existing during a range of scales. In the following, we present briefly the main steps of the primal sketch construction.

##### A. Gray-Level Blobs (GLBs)

At each level of scale (i.e., diffusion time  $t$ ), some 2-D objects called *gray-level blobs* (GLBs) are extracted from the smoothed curvature map. Each GLB is a basin, which may represent a cortical fold at this level of scale. One GLB is defined for each local minimum. The GLBs spatial extent (a set of lattice nodes) is defined from a water rise like algorithm. The water pouring from each minimum fills a basin, which altitude is defined by the lowest surrounding saddle point (see Fig. 4). In practice, each minimum is given a different label that marks a growing area. The growing is performed altitude by altitude, following

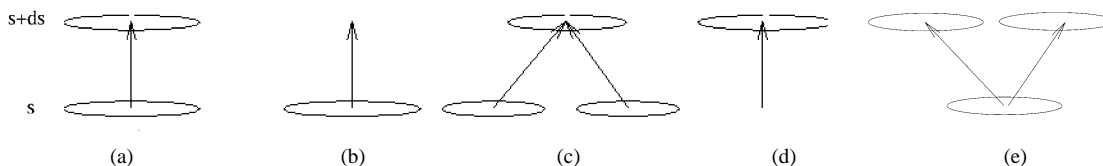


Fig. 5. The basic matching relations between GLBs through the scales. (a) Plain link. (b) Annihilation. (c) Merge. (d) Creation. (e) Split. The GLBs are connected in a SSB with *plain links*.

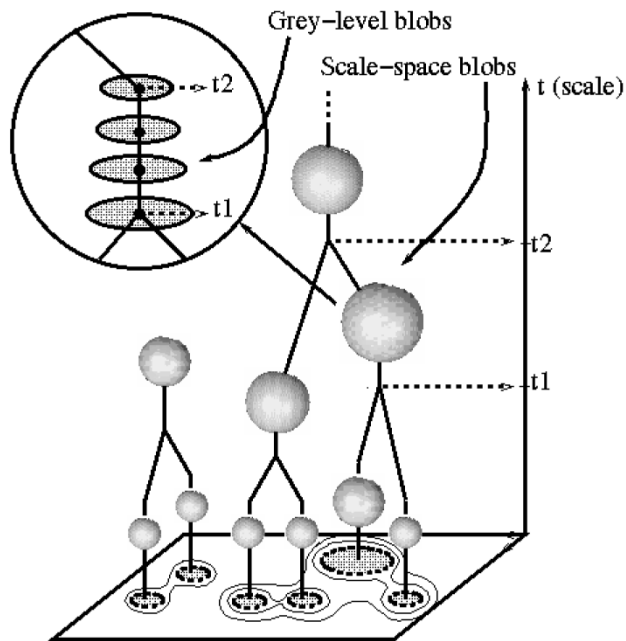


Fig. 6. Definition of the SSBs from the GLBs. GLBs belonging to the same chain can be seen as different instances of a same SSB. The organization of the primal sketch in the space and through the scale yields an explicit structural multiscale description of the sulcal topography (from Coulon *et al.* [67]).

the water rise idea. An area begins to grow when it is reached by the water. When two growing areas with different labels get in touch, their growing is stopped. The surrounding areas, however, are marked by a background label and the background follows the water rise. When a growing area gets in touch with the background area, its growing is stopped too. When the highest altitude has been reached, the lattice is made up of GLB supports and background area. Inverting the rise of water could allow the definition of some GLBs for each local maximum, which could also be of interest to study the gyral patterns.

*B. Scale-Space Blobs (SSBs)*

Each GLB is defined by two extremal points, a local minimum and a saddle point, whose behaviors in the scale-space are well known from a theoretical point of view. The GLBs appear or disappear according to four possible events called *bifurcations*: 1) *creation* (a GLB appears); 2) *annihilation* (a GLB disappears); 3) *merge* (two GLBs merge into one); and 4) *split* (one GLB splits into two GLBs) (see Fig. 5). Between two of these events, it is possible, with a spatial overlap criterion, to track a GLB from one scale to a slightly coarser or finer one. The chains of GLBs linking two bifurcations (see Fig. 6) define multiscale objects called *scale-space blobs* (SSBs), which

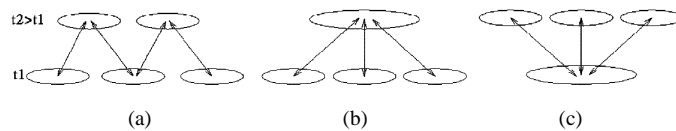


Fig. 7. Iterative construction of the scale space. Example of cases requiring an adaptive sampling.

are expected to correspond to some anatomical structures embedded in the curvature map.

*C. Adaptive Sampling of the Scale Space*

Due to the discrete sampling of the scale parameter, situations different from the five described in Fig. 5 may occur (see Fig. 7). In this case, an adaptive sampling provides an intermediate scale level at which this problematic situation can be overcome. Events in the linear scale space have been shown to arise logarithmically: the computed intermediate scale  $t$  between  $t_1$  and  $t_2$  verifies, then:  $\ln(t) = \ln(t_1) + \ln(t_2)/2$ , i.e.,  $t = \sqrt{t_1 * t_2}$ . A limit in the number of successive refinements must be fixed, and it may happen that this number is not sufficient to solve a particular problematic situation. However, reaching the limit in the number of successive refinements is not of great importance since the missed SSBs have an extremely short “lifetime” and can then be considered as not significant [42].

V. RESULTS AND DISCUSSION

*A. Central Sulcus Primal Sketch*

Figs. 9 and 10 provide a glimpse on the primal sketch focused on the central sulcus of an adult brain. The structure of this subsketch is consistent with our initial aims. First, the three highest SSBs are linked by an event which seems to correspond to the merge of the central sulcus sulcal roots described by neuroanatomists [21]. Second, the spatial localization of the two sulcal roots related blobs are separated by a buried gyrus, revealed by a slight deformation of the central sulcus wall, as described by the model. Moreover, the two sulcal roots have a longer life time throughout scales than noise related blobs.

A fine analysis of the lowest part of the sketch (the superior sulcal root), however, shows that some instabilities may stem from spurious *split* events induced by the elongated shape of the sulcus related blobs [41]. These splits, however, are not necessarily spurious and may be related to what we call “the castle wall effect.” Let us imagine a landscape with a castle wall shape, namely a wall with two thick towers as extremities. If the altitude of the wall is higher than the tower altitudes at the beginning of the smoothing process (a weird castle indeed), the whole

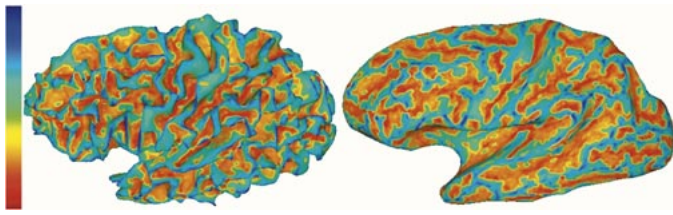


Fig. 8. Mean curvature of the cortex inner surface (adult brain), mapped on itself (left) and on an inflated version [59] (right). Red (negative) areas correspond to sulci, while blue (positive) areas correspond to gyri.

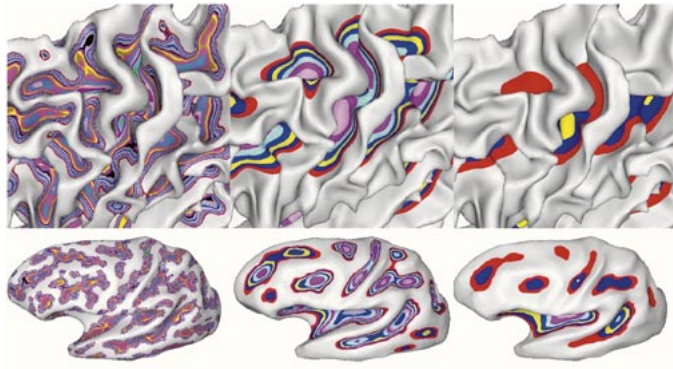


Fig. 9. Some isophotes of cortical surface mean curvature at different scales, mapped on itself (top) and on an inflated version (bottom). Central sulcus includes two curvature minima at middle scale, and finally only one minimum at highest scale. The middle scale minima will correspond to two blobs in the final primal sketch. The saddle point which separates these two blobs is located at the level of the buried gyrus related clues. Hence, these blobs may correspond to central sulcus sulcal roots.

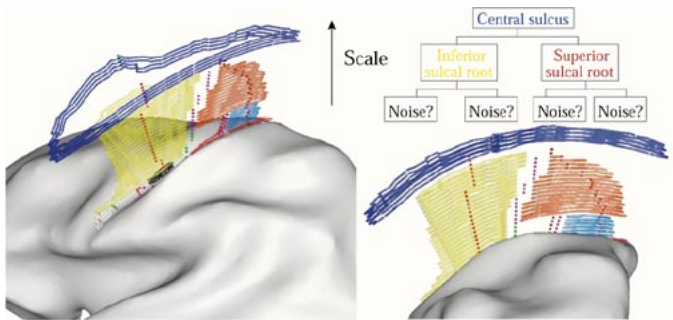


Fig. 10. Subsketch of the primal sketch focused on the central sulcus area. Each GLB is represented by its contour. The contour is moved toward the outside brain by an homothetic factor related to the logarithm of the scale. Each SSB has its own color. Red points correspond to the curvature minima from which the GLB growth begins. Purple points between two blobs and green points between one blob and the background, correspond to points stopping blob growth. The position and the organization of the SSBs located in the central sulcus zone match with the sulcal root-based model of this sulcus.

edifice is represented by only one blob. Because of their thickness, however, the tower altitudes decrease at a lower rate than the wall altitude during smoothing. Hence, after a while, the initial blob is split into two tower related blobs. It should be noted that this kind of events respects the causality property, which prevents only the creation of new level sets. When such events, however, occur because of noise induced by some weaknesses of the numerical scheme relative to the irregularity of the mesh, the primal sketch may need some postprocessing. An interesting alternative, based on a finite-element method (FEM), avoiding local planar parameterization and inversion of ill conditioned

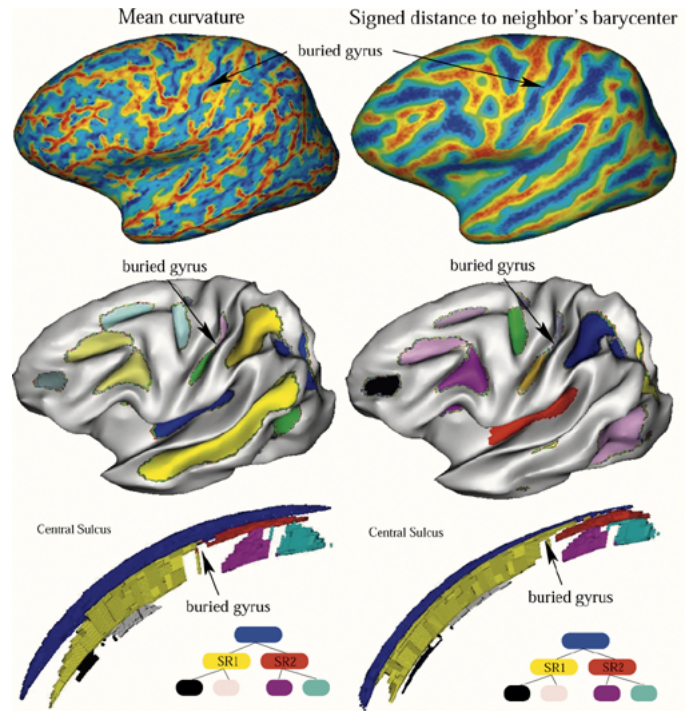


Fig. 11. Top: Two different curvature-based maps: left, the mean curvature estimation used throughout the paper; right: the signed distance to the barycenter of the neighbors in the surface mesh. Middle: The GLBs at one level of scale located before the merge of the central sulcus roots. Bottom: The structure of the upper parts of the central sulcus primal sketches are isomorphic, while the bifurcations occur at slightly different times.

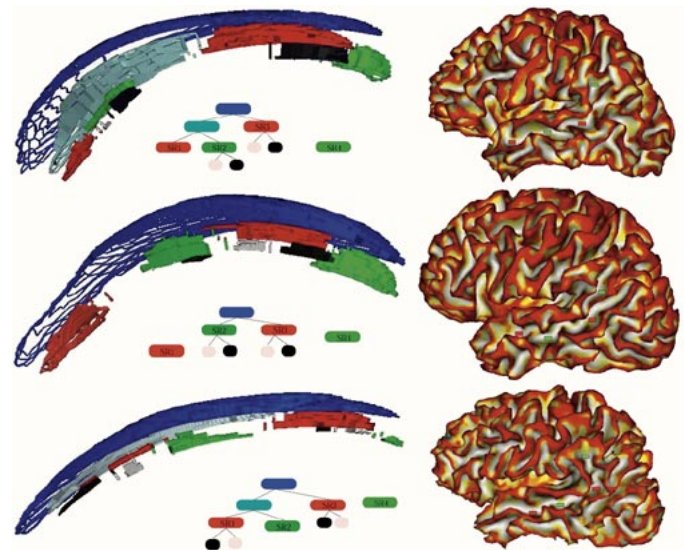


Fig. 12. Left: The part of the primal sketch corresponding to the left superior temporal sulcus for three different brains. The putative four sulcal roots of our model have been labeled in these graphs (see Fig. 1). The structure of the subsketches is slightly different across individuals, which may reflect some differences during the folding process. It should be noted that the subsketches are not necessarily connected trees, and that the superior temporal sulcus is not necessarily represented by a SSB. Right: The cortical surface of the three corresponding brains. The positive mean curvature has been mapped with a red color map in order to highlight putative gyri buried in the sulcus walls. The localizations of the curvature minima corresponding to the putative sulcal roots have been superimposed on the 3-D rendering (red and green rectangles).

matrices, can be found in [64] and is under investigation. It may overcome some of these problems.

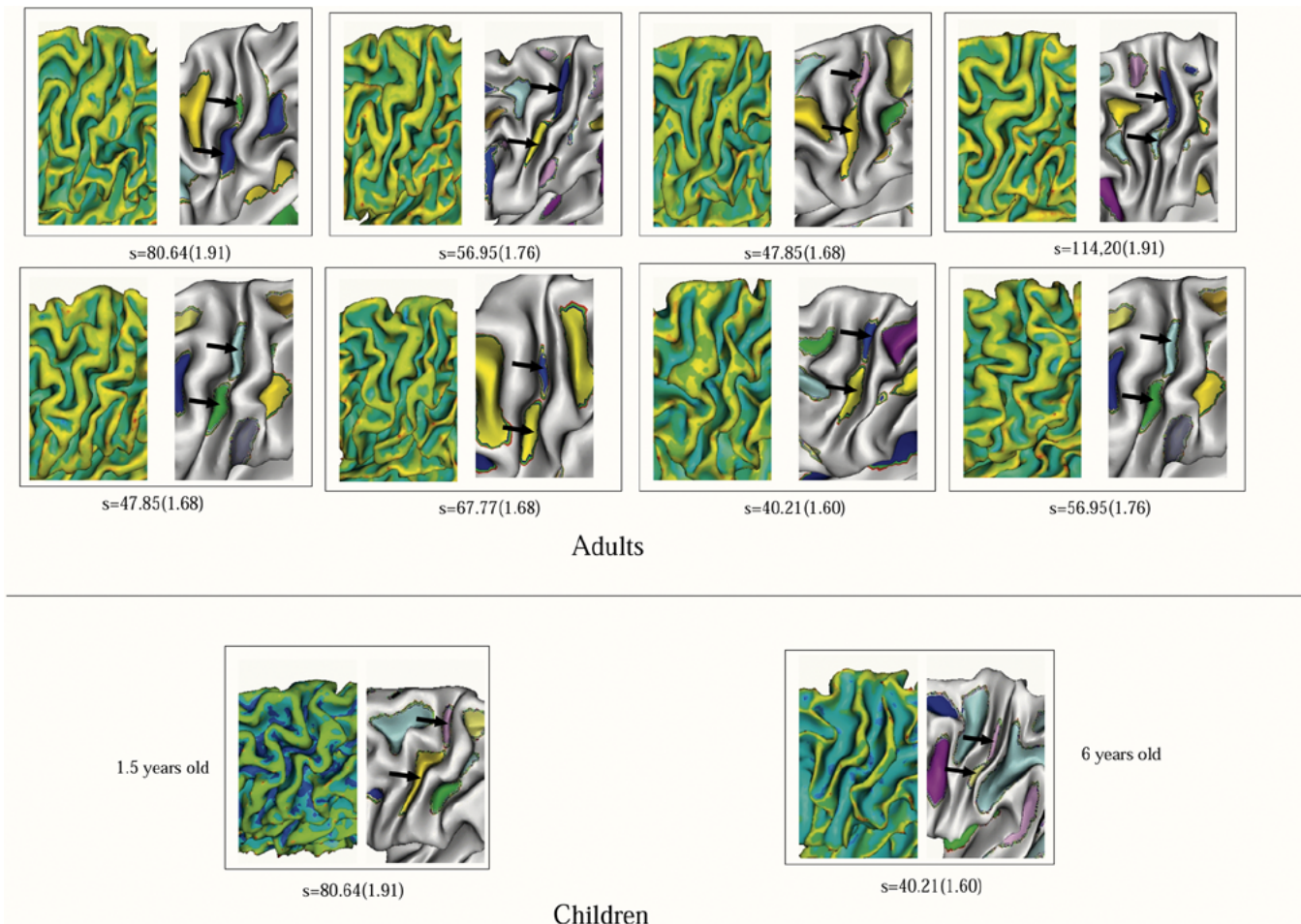


Fig. 13. Variability of the central sulcus folding pattern among eight adult (top) and two child brains (bottom). For each subject, a mesh of the cortex inner surface, mapped with its mean curvature, highlights the deep buried sulcal shape. Pinpointed blobs, mapped on a slightly inflated version of the surface, are supposed to correspond to the two putative central sulcus sulcal roots (inferior and superior); the indicated scale (with its logarithm in brackets) correspond to their scale of apparition.

### B. Stability Relative to Curvature-Based Feature

Several choices made to perform the studies described in this paper are arbitrary (mean curvature and heat equation). We hypothesize, however, that the structural anatomical information we are interested in is stable across various curvature-based features. In order to illustrate this idea, the central sulcus primal sketch computed from our mean curvature estimation has been compared to an equivalent sketch computed from a map of the distance between each node  $M$  and its mesh neighborhood barycenter  $B = \sum M_i$ , signed by the scalar product between  $\overrightarrow{MB}$  and the normal at node  $M$  (see Fig. 11). While some variability could be observed among the objects extracted at the lowest levels of scale, the highest part of the sketches rely on isomorphic sets of bifurcations defining the same candidates for the central sulcus roots.

### C. Reproducibility Across Individuals

The primal sketch has been built from ten different left hemispheres in order to check if the two sulcal root model of the central sulcus could be highlighted as an invariant of the cortex morphogenesis. The supports of the two GLBs supposed to correspond to the two putative sulcal roots are mapped on an in-

flated version of the surface, for the sake of visualization (see Fig. 13). For each brain, the scale has been chosen slightly before the event leading to the merge of the two sulcal roots into the whole central sulcus. In each case, the two GLBs are located on both sides of the central sulcus wall deformations looking like a buried gyrus. It should be noted that the spatial extent of the GLBs is not supposed to have an accurate localization power. Dedicated buried gyrus detection algorithms initialized by the localization of the GLB minima could indeed provide a better result for further studies. The goal of the primal sketch is mainly structural: highlighting the fetal structure of the adult folding patterns.

### D. Discussion

The previous results have shown that some hidden information about the morphogenesis of the cortical folding patterns could be recovered from the remaining curvature of the surface at adult age. This information could help to overcome the problems related to the interindividual variability of these patterns. Our results, however, are related to one of the simplest sulci, and more work is required to analyze whether the current primal sketch structure is sufficient to highlight a stable organization of the sulci made up of more sulcal roots. For instance, it has to be



proved that the primal sketch scale space blob set includes all the sulcal roots that have to be localized. The link between fetal sulcal roots and their putative primal sketch analogue, indeed, may be more intricate than for the central sulcus case, because several merge events are then involved. This could call for the development of more sophisticated anisotropic scale spaces.

While a first manual exploration is required to try to match the primal sketch-based representations with our current sulcal root maps (see Fig. 12), an automatic strategy should be devised to get a more reliable generic model. Few approaches have been proposed for such inference of high level models underlying the brain anatomy. Some ideas could stem from similar work done from skull crest lines [73]. Another attractive direction consists of Markovian models for the comparison of primal sketches developed to match activation maps across individuals [67]. The underlying idea consists in labeling simultaneously a large number of sketches, each label corresponding to an entity relatively stable across individuals in terms of shape, localization and surrounding. Finally, when such a sulcal root-based generic model will have been inferred from a set of brains, automatic labeling methods might be used to match it with any new primal sketch [35], [74]. It should be noted, besides, that the group analysis of geodesic scale-spaces of 2-D maps painted on the cortical surface is a generic tool, which may be of interest in other contexts such as in functional MRI/positron emission tomography studies with statistical maps [63], [67], or for the study of cortical thickness maps [68].

## VI. CONCLUSION

In this paper, we have shown that new approaches to the understanding of the variability of brain structure can be devised taking into account the variability of the brain morphogenesis. Such approaches could overcome the difficulties of iconic template-based methods to deal with structurally different patterns. The new structural multiscale-based representation of the sulcal folding patterns presented in this paper will be used to infer a finer grained than usual generic model of the human cortical surface [21], [25]. Such a model would greatly improve our current understanding of the cortex variability, and help for finding stable anatomical landmarks. These landmarks would be useful, for instance, employed as geometrical deformation constraints in warping processes [43]–[46], or for defining reliable parcellations of the cortical surface [75]. In the future, longitudinal time series of brain images will be of great help to validate our approach. Hence, long-term studies of brain growth processes will be used both as answers to neuroscience questions and as inspiration for new methodological development.

## APPENDIX

### Stability of the Numerical Scheme

The numerical resolution of the previous PDE must fulfill *convergence* and *stability* criteria to give satisfactory results.

Without loss of generality, let us consider a 1-D heat diffusion-like (parabolic) PDE

$$\frac{\partial u(x, t)}{\partial t} = K \frac{\partial^2 u(x, t)}{\partial x^2} \quad (5)$$

( $t$  is time,  $x$  the linear coordinate, and  $K$  a constant). Assuming that the temperature field (in our case the mean curvature field) is sampled by a regularly-spaced grid (with spatial sampling step  $\Delta x$ ), a finite-differences approach to approximate the partial derivatives yields

$$\frac{u_j^{n+1} - u_j^n}{\Delta t} \approx \frac{\partial u}{\partial t}(x_j, t_n) \quad (6)$$

$$\frac{u_{j+1}^n - 2u_j^n + u_{j-1}^n}{(\Delta x)^2} \approx \frac{\partial^2 u}{\partial x^2}(x_j, t_n) \quad (7)$$

where  $\Delta t$  is the temporal sampling step, and  $u_j^n$  stands for  $u(x_j, t_n)$ , i.e., the value of the function at the node  $x_j$  and at the instant  $t_n$ . Using this, approximate values  $U_j^n$  of the function (as opposed to the exact values  $u_j^n$ ) can be computed. Substituting  $U$  for  $u$  in (6) and (7), we have

$$U_j^{n+1} = U_j^n + \nu(U_{j+1}^n - 2U_j^n + U_{j-1}^n) \quad (8)$$

where  $\nu = K\Delta t/(\Delta x)^2$ .

A highly important concept in this context is the *truncation error* (so called because a truncation of a Taylor series is implied by approximations such as the ones above described) [76], [77]. The truncation error  $T_j^n$  is simply the remainder of (8) when  $U$  is replaced by the exact solution  $u$ . The numerical resolution of the PDE will be said *consistent* if the truncation error tends to zero as  $\Delta x$  and  $\Delta t$  tend to zero. In other words, consistency ensures that finer meshes and smaller iteration time steps will always lead to more accurate approximations of the actual PDE solutions at each time step and at each node.

While obviously a very desirable feature, consistency does not guarantee that the resolution will be stable. For *stability* to be attained, the actual error ( $e_j^n = U_j^n - u_j^n$ ) must tend to zero as the truncation error  $T_j^n$  tends to zero, otherwise the errors will tend to propagate rapidly and the final results will be devoid of sense. The evolution of  $e_j^n$  in time is related to the truncation error in the following way [76]:

$$e_j^{n+1} = (1 - 2\nu)e_j^n + \nu e_{j+1}^n + \nu e_{j-1}^n - T_j^n \Delta t. \quad (9)$$

The important point is that the coefficients of the terms  $e^n$  on the right add up to unity and that, provided that  $\nu \leq 1/2$ , they are all positive. This way, the error at time step  $n+1$  is bounded by  $E^n = \max\{|e_j^n|, j = 0, 1, \dots\}$  in the following way:

$$|e_j^{n+1}| \leq E^n + |T_j^n| \Delta t. \quad (10)$$

This is a sufficient condition for stability [76]. Thus, a valid numerical implementation of this simple parabolic equation would require that  $\nu = K(\Delta t/(\Delta x)^2) \leq 1/2$ .

The present case differs from the example above in two points: 1) the (2-D) mesh is not regular (nonuniform internodal separation) and 2) the estimation of the partial derivatives, although based on finite differences, relies upon the least-squares resolution of a linear system. These specificities must be accounted for in a discussion of the appropriate stability guidelines.

The PDE to solve at each node location has the form

$$\frac{\partial u(x, y, t)}{\partial t} = 0.5 \left( \frac{\partial^2 u(x, y, t)}{\partial x^2} + \frac{\partial^2 u(x, y, t)}{\partial y^2} \right). \quad (11)$$

The approximate result  $U$  satisfies

$$U_j^{n+1} - U_j^n = \frac{\Delta t}{2} \left( \frac{\partial^2 \widehat{U}_j^n}{\partial x^2} + \frac{\partial^2 \widehat{U}_j^n}{\partial y^2} \right) \quad (12)$$

where  $\partial^2 \widehat{U}_j^n / \partial x^2$  stands for “estimated partial derivative of  $U$  at node  $(x_j, y_j)$  and time point  $t_n$ ” (similarly for  $y$ ). The error  $e_j^n$  can be written as

$$e_j^n = U_j^{n+1} - \frac{\Delta t}{2} \left( \frac{\partial^2 \widehat{U}_j^n}{\partial x^2} + \frac{\partial^2 \widehat{U}_j^n}{\partial y^2} \right) - u_j^{n+1} + \frac{\Delta t}{2} \left( \frac{\partial^2 \widehat{u}_j^n}{\partial x^2} + \frac{\partial^2 \widehat{u}_j^n}{\partial y^2} \right) + T_j^n \frac{\Delta t}{2}. \quad (13)$$

Combining (13) and (4) leads to

$$e_j^{n+1} = e_j^n \left[ 1 - \frac{\Delta t}{2} \sum_{i=1}^m (A_{j_{3i}}^- + A_{j_{4i}}^-) \right] + \frac{\Delta t}{2} \sum_{i=1}^m e_{j_i}^n (A_{j_{3i}}^- + A_{j_{4i}}^-) - T_j^n \frac{\Delta t}{2} \quad (14)$$

where  $A_{j_{3i}}^-$  (respectively,  $A_{j_{4i}}^-$ ) stand for “the element contained in the third (with respect to the fourth) line and  $i$ th column of the pseudoinverse matrix pertaining to the node located at  $(x_j, y_j)$ ,” and  $e_{j_i}^n$  stands for “the error at the  $i$ th neighbor of the node located at  $(x_j, y_j)$ , at instant  $t_n$ .” A sufficient condition for the error to be bounded is that the coefficients affecting all of the  $e^n$  add up to unity (which is clearly the case) and that they are all positive. Denoting  $\omega_{j_i} = A_{j_{3i}}^- + A_{j_{4i}}^-$ , this translates as

$$\forall_j 1 - \frac{\Delta t}{2} \sum_i \omega_{j_i} > 0 \quad \text{AND} \quad \forall_{j,i} \frac{\Delta t}{2} \omega_{j_i} > 0. \quad (15)$$

From a practical point of view, these constraints apply to the elements of the  $A^-$  matrix. High elements in those lines of the  $A^-$  matrix that play a role in the estimation of the second derivatives may lead to the violation of the left-hand condition in (15) and, thus, to instability. While the analogy will not be pursued further, it is noteworthy that this constraint can be seen as putting limits to the variance of the implied least-squares estimation [78]: high-pseudoinverse values denote linear systems with unacceptably high condition numbers (nearly collinear lines in the corresponding matrix) and, therefore, high-estimation variance, liable to cause important error propagation in an iterative process.

The goal, thus, is to minimize estimation variance in order to avoid having to employ very small  $\Delta t$ 's that could ultimately require prohibitively high-computation times. With this purpose, a simple condition number minimizing algorithm was implemented at the lattice creation stage. It relies on the fact that the orientation of the referential used to define relative neighbors coordinates is arbitrary. Minimization of the condition number is performed by successively rotating the referential of the nodes that fail to comply with a user-provided threshold. In cases where two nodes are very close to each other,

this procedure may not be enough to guarantee a reasonably low value for the critical  $\Delta t$ . In such cases, an intervention at the level of the lattice configuration may be required.

For typical examples of cortical lattices submitted to node decimation (resulting number of nodes:  $\sim 20\,000$ – $25\,000$ ), the fulfillment of the left-hand condition in (15) required  $\Delta t$ 's of  $\sim 0.5$ – $0.7$ . However, practice revealed that  $\Delta t$ 's as high as one led to stable systems, showing that the error can be bounded even in cases where the sufficient condition for stability is violated.

The right-hand condition in (15) is apparently more difficult to fulfill. However, the several violations that were identified in the tested lattices were not an obstacle to a stable numerical resolution, showing that the fulfillment of the first condition is in itself enough to guarantee a satisfactory bounding of the error.

The application of postprocessing procedures (e.g., decimation) to the lattice may lead to situations in which node neighbors are fewer than the number of variables estimated locally. This number will be five in the case of the second-order Taylor expansion necessary to estimate the Laplacian, or four if isotropy is assumed and the  $\partial^2 f_0 / \partial x \partial y$  term is considered to be zero, as in the current implementation. A deficit of neighbors will lead to indeterminacy of the corresponding linear system, which means that the solution will not be unique. One of the options to pick one among the infinity of solutions, thus, obtained is to select the solution with the smallest norm. This is the condition implied by the Moore–Penrose pseudoinverse [79] based resolution that we adopted. This was shown to be a sensible option in practice: provided that the nodes with less than four neighbors constitute a small ( $\sim 1\%$ ) proportion of the total number of nodes, the final results do not differ significantly from those obtained in a situation of system determinacy all over the lattice.

## REFERENCES

- [1] M. Miller, G. E. Christensen, Y. Amit, and U. Grenander, “A mathematical textbook of deformable neuroanatomies,” *Proc. Nat. Acad. Sci. USA*, vol. 90, pp. 11 944–11 948, 1993.
- [2] P. E. Roland and K. Zilles, “Brain atlases—a new research tool,” *Trends Neurosci.*, vol. 17, pp. 458–467, 1994.
- [3] D. L. Collins, P. Neelin, T. M. Peters, and A. C. Evans, “Automatic 3D intersubject registration of MR volumetric data in standardized talairach space,” *J. Comput. Assist. Tomogr.*, vol. 18, no. 2, pp. 192–205, 1994.
- [4] K. Friston, J. Ashburner, J.-B. Poline, C. D. Frith, J. D. Heather, and R. S. J. Frackowiak, “Spatial realignment and normalization of images,” *Hum. Brain Mapp.*, vol. 2, pp. 165–189, 1995.
- [5] J. Mazziotta, A. W. Toga, A. Evans, P. Fox, and J. Lancaster, “A probabilistic atlas of the human brain: Theory and rationale for its development,” *NeuroImage*, vol. 2, pp. 89–101, 1995.
- [6] D. C. Van Essen and H. A. Drury, “Structural and functional analysis of human cerebral cortex using a surface-based atlas,” *J. Neurosci.*, vol. 17, pp. 7079–7102, 1997.
- [7] J. Ashburner and K. J. Friston, “Voxel-based morphometry—The methods,” *NeuroImage*, vol. 11, pp. 805–821, 2000.
- [8] B. Fischl, M. I. Sereno, R. B. Tootle, and A. M. Dale, “High-resolution intersubject averaging and a coordinate system for the cortical surface,” *Hum. Brain Mapp.*, vol. 8, no. 4, pp. 272–84, 1999.
- [9] P. M. Thompson, R. P. Woods, M. S. Mega, and A. W. Toga, “Mathematical/computational challenges in creating deformable and probabilistic atlases of the human brain,” *Hum. Brain Mapp.*, vol. 9, pp. 81–92, 2000.
- [10] M. K. Chung, K. J. Worsley, T. Paus, C. Cherif, D. L. Collins, J. N. Giedd, J. L. Rapoport, and A. C. Evans, “A unified statistical approach to deformation-based morphometry,” *NeuroImage*, vol. 14, no. 3, pp. 595–606, 2001.

- [11] A. Guimond, A. Roche, N. Ayache, and J. Meunier, "Multimodal brain warping using the Demons algorithm and adaptative intensity corrections," *IEEE Trans. Med. Imag.*, vol. 20, pp. 58–69, Jan. 2001.
- [12] A. W. Toga and P. M. Thompson, "New approaches in brain morphometry," *Amer. J. Geriatr. Psych.*, vol. 10, no. 1, pp. 13–23, 2002.
- [13] F. G. Woermann, S. L. Free, M. J. Koepp, J. Ashburner, and J. S. Duncan, "Voxel-by-voxel comparison of automatically segmented cerebral gray matter—a rater-independent comparison of structural MRI in patients with epilepsy," *NeuroImage*, vol. 10, pp. 373–384, 1999.
- [14] A. May, J. Ashburner, C. Buchel, D. J. McGonigle, K. J. Friston, R. S. Frackowiak, and P. J. Goadsby, "Correlation between structural and functional changes in brain in an idiopathic headache syndrome," *Nat. Med.*, vol. 5, no. 7, pp. 836–838, 1999.
- [15] E. A. Maguire, D. G. Gadian, I. S. Johnsrude, C. D. Good, J. Ashburner, R. S. Frackowiak, and C. D. Frith, "Navigation-related structural change in the hippocampi of taxi drivers," *Proc. Nat. Acad. Sci. USA*, vol. 97, no. 9, pp. 4414–6, 2000.
- [16] P. Thompson *et al.*, "Genetic influences on brain structure," *Nature Neurosci.*, vol. 4, no. 3, pp. 83–95, 2001.
- [17] C. Davatzikos and R. N. Bryan, "Morphometric analysis of cortical sulci using parametric ribbons: A study of the central sulcus," *J. Comput. Assist. Tomogr.*, vol. 26, no. 2, pp. 298–307, 2002.
- [18] T. Paus, A. Zijdenbos, K. Worthley, D. L. Collins, J. Blumenthal, J. N. Giedd, J. L. Rapoport, and A. C. Evans, "Structural maturation of neural pathways in children and adolescents: *In vivo* study," *Science*, vol. 283, pp. 1908–1911, 1999.
- [19] T. Paus, D. L. Collins, A. C. Evans, G. Leonard, B. Pike, and A. Zijdenbos, "Maturation of white matter in the human brain: A review of magnetic resonance studies," *Brain Res. Bull.*, vol. 54, no. 3, pp. 255–66, 2001.
- [20] C. D. Good, I. S. Johnsrude, J. Ashburner, R. N. Henson, K. J. Friston, and R. S. Frackowiak, "A voxel-based morphometric study of aging in 465 normal adult human brains," *NeuroImage*, vol. 14, no. 1, pp. 21–36, 2001.
- [21] J. Régis, J.-F. Mangin, V. Frouin, F. Sastre, J. C. Peragut, and Y. Samson, "Generic model for the localization of the cerebral cortex and preoperative multimodal integration in epilepsy surgery," *Stereotactic Functional Neurosurg.*, vol. 65, pp. 72–80, 1995.
- [22] D. C. Van Essen, "A tension-based theory of morphogenesis and compact wiring in the central nervous system," *Nature*, vol. 385, pp. 313–318, 1997.
- [23] M. Ono, S. Kubik, and C. D. Abernethy, *Atlas of the Cerebral Sulci*. Stuttgart, Germany: Georg Thieme Verlag, 1990.
- [24] W. Welker, "Why does the cerebral cortex fissure and fold," *Cerebral Cortex*, vol. 8B, pp. 3–135, 1989.
- [25] J. Régis, "Deep sulcal anatomy and functional mapping of the cerebral cortex (in french)," MD thesis, Université d'Aix-Marseille II, Marseille, France, 1994.
- [26] A. Manceaux-Demiau, J.-F. Mangin, J. Régis, O. Pizzato, and V. Frouin, "Differential features of cortical folds," in *Lecture Notes in Computer Science*. Berlin, Germany: Springer-Verlag, 1997, vol. 1205, Proceedings CVRMed/MRCAS Grenoble, pp. 439–448.
- [27] A. Manceaux-Demiau, R. N. Bryan, and C. Davatzikos, "A probabilistic ribbon model for shape analysis of the cerebral sulci: Application to the central sulcus," *J. Comput. Assist. Tomogr.*, vol. 22, no. 6, pp. 962–71, 1998.
- [28] F. A. Sastre-Janer, J. Régis, P. Belin, J.-F. Mangin, D. Dormont, M. C. Masure, P. Remy, V. Frouin, and Y. Samson, "Three-dimensional reconstruction of the human central sulcus reveals a morphological correlate of the hand area," *Cerebral Cortex*, vol. 8, no. 7, pp. 641–7, 1998.
- [29] Y. G. Le Goualher, A. M. Argenti, M. Duyme, W. F. Baare, H. E. Hulshoff Pol, D. I. Boomsma, A. Zouaoui, C. Barillot, and A. C. Evans, "Statistical sulcal shape comparisons: Application to the detection of genetic encoding of the central sulcus shape," *NeuroImage*, vol. 11, no. 1, pp. 564–74, 2000.
- [30] D. Cunningham, *Contribution to the Surface Anatomy of the Cerebral Hemispheres*. Dublin, Ireland: Academy House, 1892.
- [31] D. Waterson, "Complete bilateral interruption of the fissure orlando," *J. Anat.*, vol. 41, pp. 43–146, 1907.
- [32] T. A. Yousry, U. D. Schmid, H. Alkadhi, D. Schmidt, A. Peraud, A. Buettner, and P. Winkler, "Localization of the motor hand area to a knob on the precentral gyrus. A new landmark," *Brain*, vol. 120, no. 1, pp. 141–57, 1997.
- [33] L. E. White, T. J. Andrews, C. Hulette, A. Richards, M. Groelle, J. Paydarfar, and D. Purves, "Structure of the human sensorimotor system. I: Morphology and cytoarchitecture of the central sulcus," *Cerebral Cortex*, vol. 7, no. 1, pp. 18–30, 1997.
- [34] W. Boling, A. Olivier, R. G. Bittar, and D. Reutens, "Localization of hand motor activation in broca's pli de passage moyen," *J. Neurosurg.*, vol. 91, no. 6, pp. 903–10, 1999.
- [35] G. Lohmann and D. Y. von Cramon, "Automatic labeling of the human cortical surface using sulcal basins," *Med. Image Anal.*, vol. 4, no. 3, pp. 179–188, 2000.
- [36] M. E. Rettman, X. Han, C. Xu, and J. L. Prince, "Automated sulcal segmentation using watersheds on the cortical surface," *NeuroImage*, vol. 15, pp. 329–344, 2002.
- [37] D. Marr, *Vision*. New York: Freeman, 1982.
- [38] H. Jasada and M. Brady, "The curvature primal sketch," *IEEE Pattern Anal. Machine Intell.*, vol. PAMI-8, pp. 2–14, 1986.
- [39] A. Witkin, "Scale-space filtering," in *Proc. Int. Joint Conf. Artificial Intelligence*, 1983, pp. 1019–1023.
- [40] J. Koenderink and A. van Doorn, "The structure of images," *Biol. Cybern.*, vol. 53, pp. 383–396, 1984.
- [41] L. Lifshitz and S. Pizer, "A multiresolution hierarchical approach to image segmentation based on intensity extrema," *IEEE Trans. Pattern Anal. Machine Intell.*, vol. 12, pp. 529–540, June 1990.
- [42] T. Lindeberg, "Detecting salient blob-like image structures and their scales with a scale-space primal sketch: A method for focus-of-attention," *Int. J. Comput. Vis.*, vol. 11, no. 3, pp. 283–318, 1993.
- [43] P. Thompson and A. W. Toga, "Detection, visualization and animation of abnormal anatomic structure with a deformable probabilistic brain atlas based on random vector field transformation," *Med. Image Anal.*, vol. 1, no. 4, pp. 271–294, 1996.
- [44] D. L. Collins, D. L. Le Goualher G, and A. C. Evans, "Non-linear cerebral registration with sulcal constraints," in *Lecture Notes in Computer Science*. Berlin, Germany: Springer-Verlag, 1998, vol. 1496, Proceedings MICCAI'98, pp. 974–984.
- [45] M. Vaillant and C. Davatzikos, "Hierarchical matching of cortical features for deformable brain image registration," in *Lecture Notes in Computer Science*. Berlin, Germany: Springer-Verlag, 1999, vol. 1613, Proceedings IPMI'99, pp. 182–195.
- [46] P. Cachier, J.-F. Mangin, X. Pennec, D. Rivière, D. Papadopoulos-Orfanos, J. Régis, and N. Ayache, "Multisubject nonrigid registration of brain MRI using intensity and geometric features," in *Lecture Notes in Computer Science*, W. J. Niessen and M. A. Viergever, Eds. Berlin, Germany: Springer-Verlag, Oct. 2001, vol. 2208, Proc. 4th Int. Conf. Medical Image Computing and Computer-Assisted Intervention (MICCAI'01), pp. 734–742.
- [47] N. Royackkers, M. Desvignes, H. Fawal, and M. Revenu, "Detection and statistical analysis of human cortical sulci," *NeuroImage*, vol. 10, pp. 625–641, 1999.
- [48] G. Le Goualher, C. Barillot, and Y. Bizais, "Modeling cortical sulci using active ribbons," *Int. J. Pattern Recogn. Artific. Intell.*, vol. 11, no. 8, pp. 1295–1315, 1997.
- [49] M. Vaillant and C. Davatzikos, "Finding parametric representations of the cortical sulci using active contour model," *Med. Image Anal.*, vol. 1, no. 4, pp. 295–315, 1997.
- [50] J.-F. Mangin, "Entropy minimization for automatic correction of intensity non uniformity," in *Proc. MMBIA*, 2000, pp. 162–169.
- [51] J.-F. Mangin, O. Coulon, and V. Frouin, "Robust brain segmentation using histogram scale-space analysis and mathematical morphology," in *Lecture Notes in Computer Science, MIT, LNCS*. Berlin, Germany: Springer-Verlag, 1998, vol. 1496, Proceedings MICCAI'98, pp. 1230–1241.
- [52] J.-F. Mangin, J. Régis, and V. Frouin, "Shape bottlenecks and conservative flow systems," in *Proc. IEEE/SIAM Workshop on Mathematical Methods in Biomedical Image Analysis*, 1996, pp. 319–328.
- [53] J.-F. Mangin, V. Frouin, I. Bloch, J. Régis, and J. López-Krahe, "From 3D MR images to structural representations of the cortex topography using topology preserving deformations," *J. Math. Imag. Vis.*, vol. 5, no. 4, pp. 297–318, 1995.
- [54] D. Gordon and J. Udupa, "Fast surface tracking in three-dimensional binary images," *Comput. Vis. Graph. Image Processing*, vol. 45, no. 6, pp. 196–214, 1989.
- [55] W. Schroeder, J. Zarge, and W. Lorensen, "Decimation of triangle meshes," in *Proc. SIGGRAPH'92*, 1992, pp. 65–70.
- [56] R. Heidemann, M. Griswold, C. Hillenbrand, D. Hanh, A. Haase, and P. Jakob, "Establishing T2-contrast in true FISP imaging," in *Proc. ISMRM'01*, Apr. 2001.
- [57] K. P. Pruessmann, M. Weiger, M. W. Scheidegger, and P. Boesiger, "SENSE: Sensitivity encoding for fast MRI," *Magn. Reson. Med.*, vol. 42, pp. 952–962, 1999.
- [58] J. A. Sethian, *Level Set Methods*. Cambridge, U.K.: Cambridge Univ. Press, 1996.

- [59] H. A. Drury, D. C. Van Essen, X. H. Anderson, C. W. Lee, T. A. Coogan, and J. W. Lewis, "Computerized mappings of the cerebral cortex: A multiresolution flattening method and a surface based coordinate system," *J. Cogn. Neurosci.*, vol. 8, no. 1, pp. 1–28, 1996.
- [60] E. Boix, "Approximation lineaire des surfaces de  $R^3$  et applications," Ph.D. dissertation, Ecole Polytechnique, France, 1995.
- [61] P. Veron, D. Lesage, and J.-C. Leon, "Outils de base pour l'extraction de caracteristiques de surfaces numerisees," *7eme assises europeene du prototypage rapide—Ecole Centrale de Paris*, 1998.
- [62] A. Cachia, J.-F. Mangin, N. Boddaert, J. Régis, F. Kherif, P. Sonigo, M. Zilbovicius, I. Bloch, and F. Brunelle, "Study of cortical folding process with prenatal MR imaging," in *Proc. ISMRM'01*, Apr. 2001.
- [63] A. Andrade, F. Kherif, J.-F. Mangin, K. J. Worsley, A. L. Paradis, O. Simon, S. Dehaene, S. D Le Bihan, and J.-B. Poline, "Detection of fMRI activation using cortical surface mapping," *Hum. Brain Mapp.*, vol. 12, no. 2, pp. 79–93, 2001.
- [64] M. K. Chung, J. Taylor, K. J. Worsley, J. O. Ramsay, S. Robbins, and A. Evans, "Diffusion smoothing on the cortical surface via the laplace-beltrami operator," *IEEE Trans. Med. Imag.*, submitted for publication.
- [65] L. D. Griffin, "The intrinsic geometry of the cerebral cortex," *J. Theor. Biol.*, vol. 166, pp. 261–273, 1994.
- [66] N. Sochen, R. Kimmel, and R. Malladi, "A general framework for low level vision," *IEEE Trans. Image Processing*, vol. 20, pp. 100–107, Mar. 1999.
- [67] O. Coulon, J.-F. Mangin, J.-B. Poline, M. Zilbovicius, D. Roumenov, Y. Samson, V. Frouin, and I. Bloch, "Structural group analysis of functional activation maps," *NeuroImage*, vol. 11, pp. 767–782, 2000.
- [68] B. Fischl and A. M. Dale, "Measuring the thickness of the human cerebral cortex from magnetic resonance images," *Proc. Natl. Acad. Sci. USA*, vol. 97, no. 20, pp. 11 050–5, 2000.
- [69] W. Welch and A. Witkin, "Free-form shape design using triangulated surfaces," in *Proc. SIGGRAPH '94, Computer Graphics Proc., Annu. Conf. Series*, July 1994, pp. 247–256.
- [70] X. Tao, J. L. Prince, and C. Davatzikos, "Using a statistical shape model to extract sulci curves on the outer cortex of the human brain," *IEEE Trans. Med. Imag.*, vol. 21, pp. 513–524, May 2002.
- [71] T. Liszka and J. Orkisz, "The finite difference method at arbitrary irregular grids and its applications in applied mechanics," *Comput. Structures*, vol. 11, pp. 83–95, 1980.
- [72] G. Huiskamp, "Different formulas for the surface laplacian on a triangulated surface," *J. Comput. Phys.*, vol. 95, pp. 477–496, 1991.
- [73] G. Subsol, J. P. Thirion, and N. Ayache, "A scheme for automatically building three-dimensional morphometric anatomical atlases: Application to a skull atlas," *Med. Image Anal.*, vol. 2, no. 1, pp. 37–60, 1998.
- [74] D. Riviere, J.-F. Mangin, D. Papadopoulos-Orfanos, J.-M. Martinez, V. Frouin, and J. Régis, "Automatic recognition of cortical sulci of the human brain using a congregation of neural networks," *Med. Image Anal.*, vol. 6, no. 2, pp. 77–92, 2002.
- [75] A. Cachia, J.-F. Mangin, D. Rivière, D. Papadopoulos-Orfanos, I. Bloch, and J. Régis, "Gyral parcellation of the cortical surface using geodesic voronoi diagrams," in *Lecture Notes in Computer Science*. Berlin, Germany: Springer-Verlag, 2002, vol. 2488, Proc. MICCAI '02, pp. 427–434.
- [76] K. W. Morton and D. F. Mayers, *Numerical Solution of Partial Differential Equations*. Cambridge, U.K.: Cambridge Univ. Press, 1994.
- [77] G. Sewell, *The Numerical Solution of Ordinary and Partial Differential Equations*. New York: Academic, 1988.
- [78] R. Christensen, *Plane Answers to Complex Questions—The Theory of Linear Models*. New York: Springer-Verlag, 1996.
- [79] J. R. Schott, *Matrix Analysis for Statistics*. New York: Wiley, 1997.